

SIMULATION MODEL CALIBRATION USING SYSTEM IDENTIFICATION FOR A VECTORED-THRUST MULTI-TILT-ROTOR CONFIGURATION

Bikash Kunwar[1], Stefanus Putra[1], Rajan Bhandari[1], Cole McCormick[1] & Imon Chakraborty[1]

[1]Vehicle Systems, Dynamics, and Design Laboratory, Department of Aerospace Engineering, Auburn University, Auburn, AL, USA

Abstract

This paper presents the results of preliminary system identification that has been performed by the Vehicle Systems, Dynamics, and Design Laboratory on the VT-03-s Shadow multi-tiltrotor subscale aircraft. The effort was concentrated on the hover flight condition, with limited data collected in translational flight. In addition to continuously varying frequency sweeps, constant frequency excitations at discrete frequencies within the same frequency range were conducted for each axis. Sequential step input commands were also used to evaluate the response of the aircraft. Based on the flight data collected, on-axis transfer functions as well as lower-order equivalent systems for explicit model-following inner-loop controller design were identified. Comparisons between flight-test data and simulation results from the aircraft flight simulation model identified some areas where agreement was acceptable. However, it also highlighted other areas where the aero-propulsive modeling in the simulation model is currently deficient and must be calibrated or refined based on the collected flight-test data in future work to address these deficiencies.

Keywords: simulation, subscale flight-testing, system identification, calibration, aero-propulsive

1. Introduction

The Vehicle Systems, Dynamics, and Design Laboratory (VSDDL) developed the VT-03-s Shadow multi-tiltrotor subscale aircraft (Fig. 1, Fig. 2) based on the RAVEN configuration being analyzed by NASA and Georgia Tech researchers [1–3]. The development program for Shadow included the development of a computationally tractable aero-propulsive performance model (APPM) that enabled real-time closed-loop flight simulation of the aircraft and its flight control laws. The simulation capability was a key enabler for a rapid development cycle, in particular, the development of novel control laws that have been successfully demonstrated through flight-testing [4].

Recently, a system identification campaign focusing on the hover flight condition has been performed with VT-03-s Shadow. System identification presents an effective method of identifying the aircraft dynamics model. In both the time domain and the frequency domain, it is extensively used to obtain the dynamic model of full-scale aircraft and, more recently, subscale aircraft, including novel configurations [5–8]. System identification techniques were applied to identify the on-axis transfer functions for roll, pitch, yaw, and heave axes at the hover flight condition. Limited data was also gathered on nacelle angle versus airspeed during translational flight. This paper presents the identified on-axis transfer functions and lower-order equivalent system models and compares the identified aircraft characteristics with the corresponding predictions from its simulation model.

In the following,an overview of the VT-03-s Shadow aircraft, modeling and simulation approach, and flight-testing setup are provided in Section 2. The system identification approach is described in Sec. 3. Flight-testing results and comparisons to simulation are provided in Section 4. Conclusions and avenues for future work are identified in Section 5.

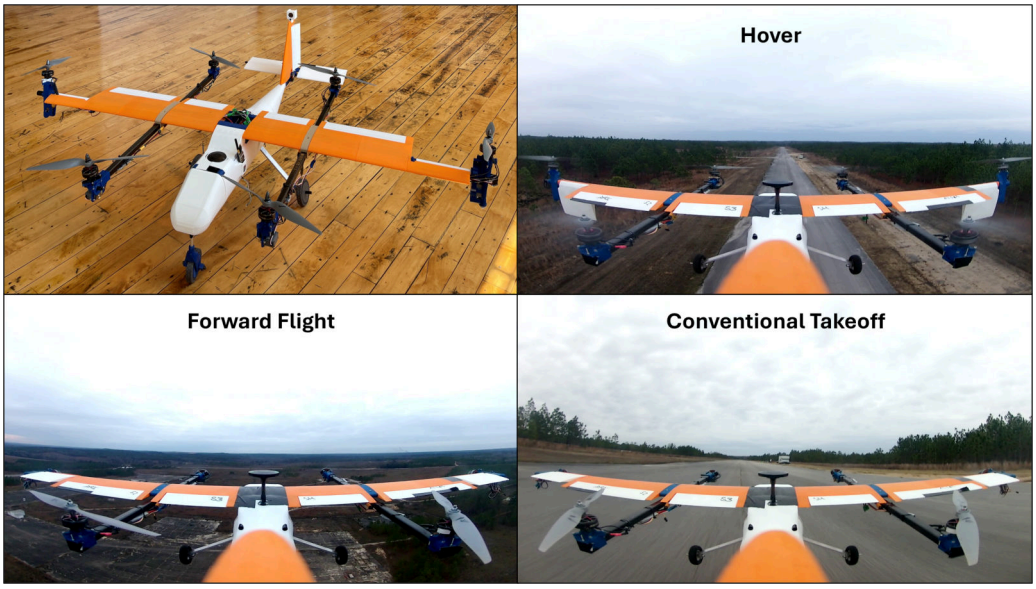


Figure 1 – VT-03-s Shadow subscale aircraft

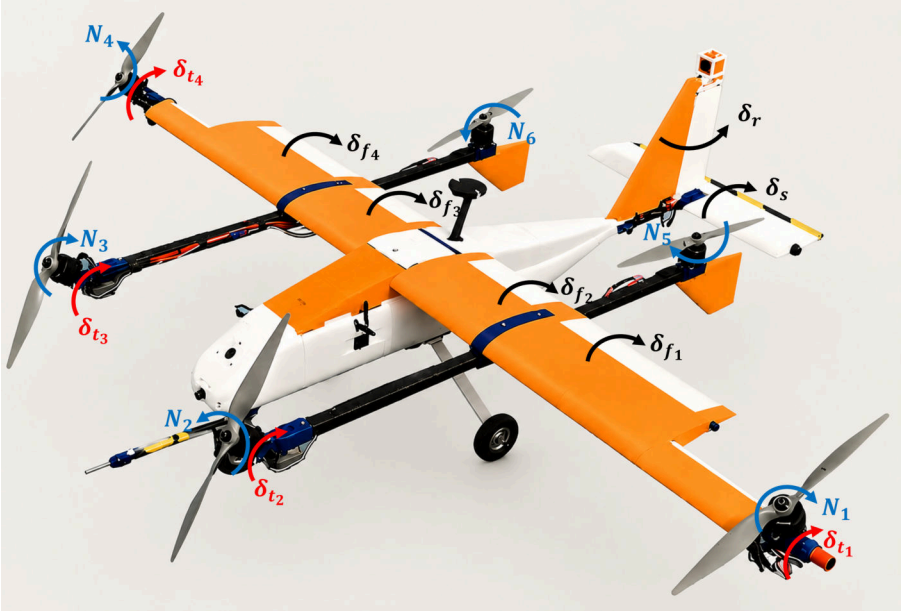


Figure 2 – VT-03-s Shadow control effector definitions

2. Aircraft Configuration, Modeling & Simulation, and Flight-Testing Setup

The VT-03-s Shadow, shown in Fig. 1, is a vectored thrust multi-tiltrotor subscale aircraft based on the RAVEN configuration described by Georgia Tech and NASA researchers [2, 3, 9]. It has a high-wing, conventional tail with stabilator, and a fixed tricycle landing gear with a castering nosewheel. The major characteristics of the aircraft are in Table 1. It has 16 control effectors as marked in Fig. 2 and listed in Table 2. The aircraft is capable of both vertical takeoff and landing (VTOL) and conventional takeoff and landing (CTOL) operating modes.

In vertical flight, the main propulsors are oriented vertically. Differential thrust between propulsors (1,2,5) and (3,4,6) is used for roll control. Differential thrust between (2,3) and (5,6) is used for pitch control. Yaw is controlled by the differential tilt of the wingtip propulsors 1 and 4. As the aircraft accelerates, the main propulsors progressively tilt forward.

In forward flight and for CTOL operations, the main propulsors assume a horizontal orientation, and the lift propulsors are inactive. The inboard and midboard flaperons on the wing are used for roll control, an all-moving stabilator is used for pitch control, and a rudder on the vertical stabilizer is

Table 1 – VT-03-s Shadow - key characteristics

Propulsion	
Motors ($\times$6)	SunnySky XS X4112S KV450
Main Propeller ($\times$4)	APC 15$\times$10 E/EP fixed-pitch
Lift Propeller ($\times$2)	APC 15$\times$4 E/EP fixed-pitch
Main Battery	Hoovoo 10000 mAh 6S LiPo
Avionics Battery	HRB 3000 mAh 4S LiPo
ESC	Zubax Myxa B
Avionics & Sensors	
Flight Controller	CubePilot Cube Orange
GPS	Here3+ GPS
Airspeed Sensor	MATEKSYS ASPD-4525
LiDAR	TFmini-S
Telemetry	RFD 900X-US
FPV	Walksnail Avatar GT digital
Geometry	
Wingspan	1.7 m / 5.6 ft
Length	1.32 m / 4.32 ft (excluding pitot)
Length	1.60 m / 5.24 ft (including pitot)
Mass Properties	
Gross Weight	8.18 kg / 18.03 lb
Body-fixed axes	forward-right-down
Origin	Nacelle 1,4 pivot axis on centerline
x_{cg}, y_{cg}, z_{cg}	$\{0, 0, 6.20\}$ cm / $\{0, 0, 2.44\}$ in
Inertias I_{xx}, I_{yy}, I_{zz}	1.35, 0.82, 1.72 kg·m^2

Table 2 – VT-03-s Shadow control effectors

#	Symbol	Description	Unit
1	δ_{f_1}	Flaperon, left wing, midboard	deg
2	δ_{f_2}	Flaperon, left wing, inboard	deg
3	δ_{f_3}	Flaperon, right wing, inboard	deg
4	δ_{f_4}	Flaperon, right wing, midboard	deg
5	δ_s	Stabilator	deg
6	δ_r	Rudder	deg
7	δ_{t_1}	Nacelle tilt angle, left wingtip	deg
8	δ_{t_2}	Nacelle tilt angle, front left boom	deg
9	δ_{t_3}	Nacelle tilt angle, front right boom	deg
10	δ_{t_4}	Nacelle tilt angle, right wingtip	deg
11–14	N_1–N_4	Main propeller RPMs	RPM
15–16	N_5, N_6	Lift propeller RPMs	RPM

used for yaw control. When operating on the ground in CTOL mode, differential thrust from the forward-facing main propulsors allows ground steering.

Additive manufacturing (3D-printing) is used to fabricate the aerodynamic surfaces and some structural components. Lightweight Polylactic Acid (LW-PLA) is used as the print material for the aerodynamic surfaces and non-structural components. Polylactic Acid plus (PLA+), a stronger variant of Polylactic Acid (PLA), is used to fabricate the structural components of the vehicle.

2.1 MADCASP Flight Simulation Model

The MATLAB/Simulink-based *Modular Aircraft Dynamics and Control Algorithm Simulation Platform* (MADCASP) is used for trim analysis, model linearization, and dynamic stability analysis of both

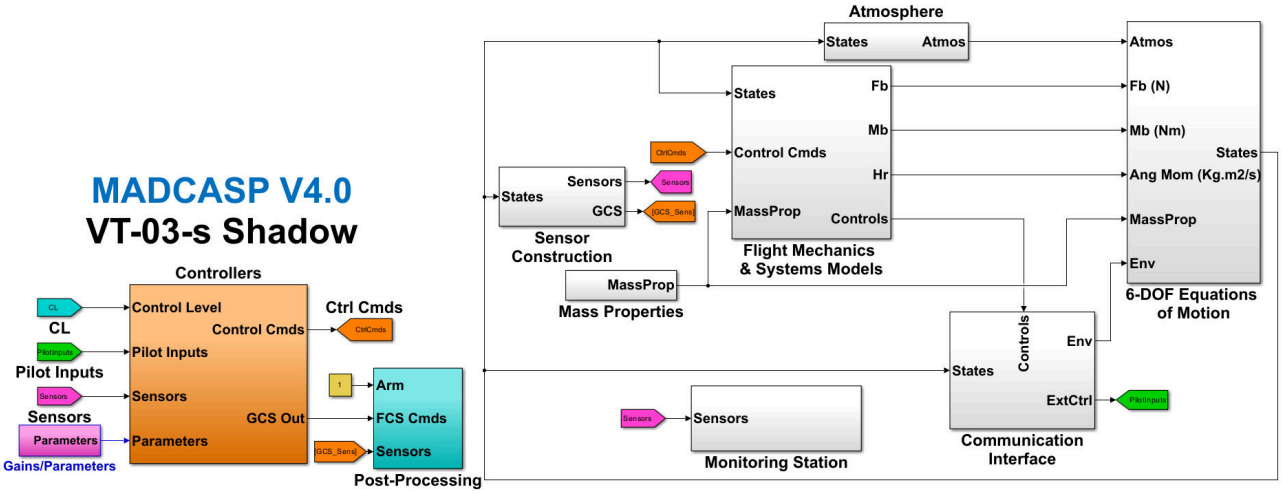


Figure 3 – Top level of MADCASP simulation model

the open-loop (bare airframe) and closed-loop systems, which facilitates controller development. A top-level of the MADCASP Simulink model for VT-03-s Shadow is shown in Fig. 3. For time-domain simulations, the Simulink model is time-marched in real time using a 4th-order Runge-Kutta scheme with a time step of 1/60 seconds (60 Hz).

2.2 Aero-propulsive Performance Model (APPM)

Within the APPM, a build-up approach is used to compute the aero-propulsive loads on the aircraft in a computationally tractable manner that allows real-time flight simulation with a 1/60 second timestep (60 Hz). For lifting surfaces, a strip theory-based approach is used, where spanwise sections are analyzed for lift, drag, and pitching moments as a function of angle of incidence (extended to a wide range of angles of attack using the Viterna equations) [10, 11]. Downwash distributions over lifting surfaces are represented using a reduced-order model (ROM) that includes geometric and aerodynamic parameters such as aspect ratio, taper ratio, and sweep [12]. Control surfaces are analyzed similarly, with adjustments for the impact of deflection and spanwise positioning on lift and drag contributions [13]. For non-lifting components such as the fuselage and nacelles, lookup tables generated using FlightStream® are used to compute aerodynamic loads as a function of angle of attack and sideslip. Landing gear drag is determined empirically.

For propulsor loads, a blade element momentum theory (BEMT) propeller model coupled to a 7-state Pitt-Peters dynamic inflow model with wake distortion effects [14] is used. Inflow dynamics are modeled using three states representing mean induced inflow, longitudinal inflow gradient, and lateral inflow gradient. Wake distortion is modeled using a further four states representing wake skew, spacing, longitudinal, and lateral wake curvature. For subscale aircraft, the BEMT model is calibrated against manufacturer propeller performance data [15] using a gradient-based optimizer to determine calibration factors to minimize the difference between published and predicted thrust and power at different RPMs and advance ratios.

For the propeller slipstream, a semi-empirical propeller slipstream model is used to determine the modification to the freestream velocity and incidence angle caused by propellers (1-4) on wing strips present downstream of them. Additional details regarding the slipstream model are provided in prior work by the authors [11].

Aero-propulsive loads computed as described above are summed over the aircraft geometry, and moments are translated to the moment reference center to obtain net aero-propulsive reactions along the body axes. This APPM approach, though not very high-fidelity, captures the aero-propulsive characteristics of novel configurations sufficiently well to allow the flight simulation model to be used for control law development. This has been demonstrated through successful flight-test demonstrations of several transitioning VTOL configurations.

2.3 Dual-Purpose Ground Control Station (GCS)

The dual-purpose GCS functions in flight-test mode in the field to interface with the subscale aircraft and in simulation mode in the laboratory to interface with its MADCASP simulation model. A high-level overview of the communication architecture in both operating modes is shown in Fig. 4.

In flight test mode, a first-person view (FPV) camera feed from the aircraft is shown on the top screen. The lower touchscreens are driven by telemetry from the vehicle. The remote pilot-in-command stands beside the GCS maintaining visual line-of-sight with the vehicle and is capable of assuming control via R/C transmitter in case of a vehicle-GCS communication failure. The flight-test engineer monitors the vehicle states on duplicate displays and can tune specific controller gains in-flight.

In simulation mode, the GCS is interfaced with the MADCASP flight simulation model. The FPV display shows a rendering of the flight environment using X-Plane Flight Simulator for visualization and terrain elevation feedback. The GCS is used in simulation mode to test, verify, and de-risk planned maneuvers and flight profiles prior to executing them in the field during flight-testing.

2.4 Flight Control Architecture

The top-level FCS architecture is shown in Fig. 5. Only a brief overview is provided in this paper and for additional details, the interested reader is referred to [4].

The pilot uses hand and foot inceptors mounted in the GCS to generate $\delta_{lat}, \delta_{ver}, \delta_{dir}, \delta_{spd} \in [-1, +1]$ normalized inputs to the FCS. The pilot can also engage automatic flight functions (e.g., automatic navigation along predefined waypoints) using touch-screen buttons on the GCS panel. A number of *holds* (pilot relief functions) for maintaining altitude, heading, ground track, position (during hover), bank, and flightpath angle engage or disengage based on inceptor positions and aircraft states.

The Maneuver Control System (MCS) is a middle-loop controller comprising two control modes: Tra-

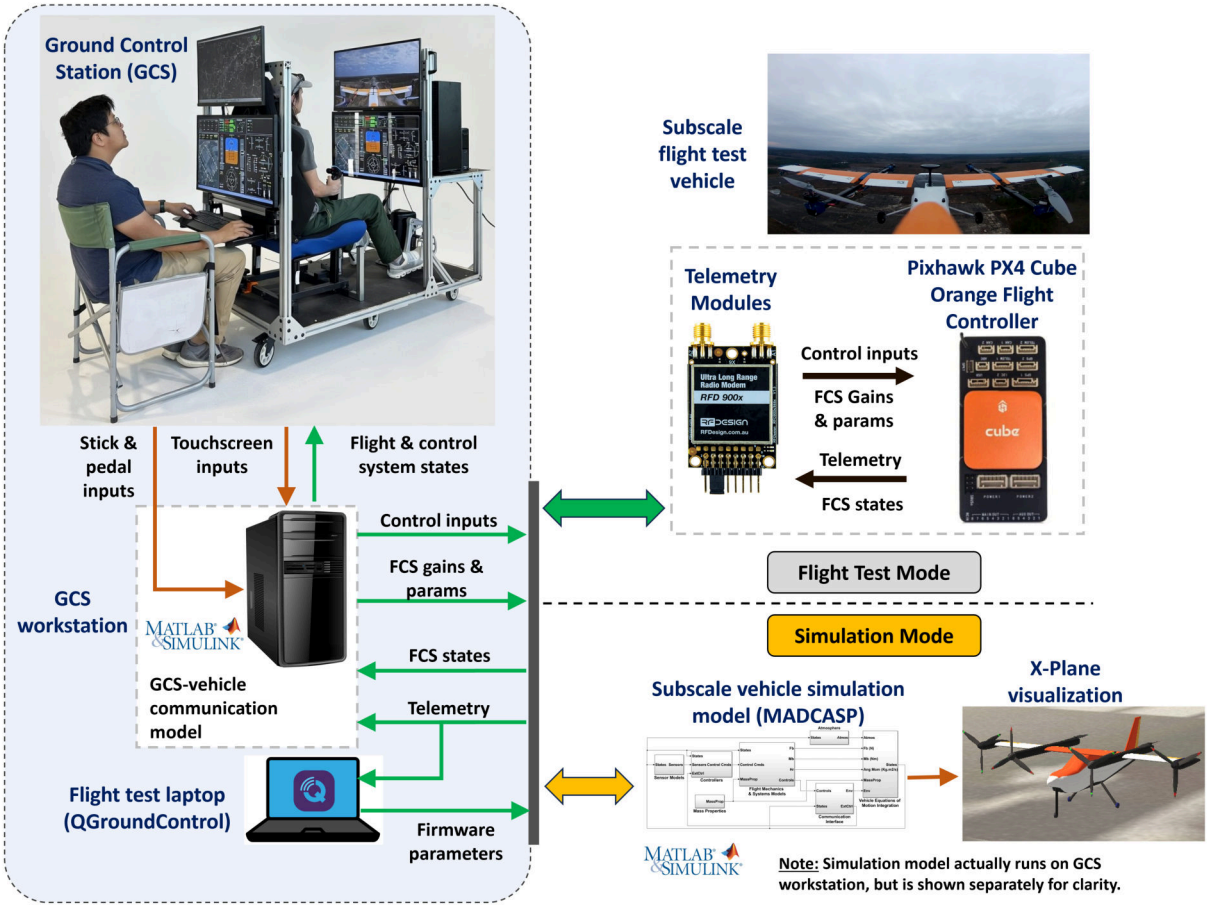


Figure 4 – GCS-vehicle and GCS-simulation connectivity

jectory Control System (TCS), intended for pilot-friendly Simplified Vehicle Operations (SVO), and Tactical Maneuvering System (TMS), intended to enable more aggressive maneuvering. The TCS and TMS control actions depend on whether the aircraft is in hybrid flight mode (HFM), transition flight mode (TFM), and forward flight mode (FFM). In HFM, the aircraft weight is supported by a combination of thrust and aerodynamic lift. In FFM, the aircraft is wingborne. TFM is a brief transitory mode connecting HFM and FFM.

The horizontal axis command to the MCS, $\xi_{H,\text{cmd}} = \left\{ \left(\dot{V}/g\right)_{\text{cmd}}, \delta_{nac,\text{cmd}}, \delta_{p,\text{cmd}} \right\}$, can comprise normalized acceleration command $(\dot{V}/g)_{\text{cmd}}$ (TCS, all flight modes), nacelle command $\delta_{nac,\text{cmd}}$ (TMS in HFM and TFM), or main propulsor power setting command $\delta_{p,\text{cmd}}$ (TMS in TFM and FFM). The vertical axis command, $\xi_{V,\text{cmd}} = \left\{ \dot{h}_{\text{cmd}},\ \Delta(T/W)_{\text{cmd},V},\ q_{\text{cmd}} \right\}$, can comprise vertical velocity command $\dot{h}_{\text{cmd}}$ (TCS, all flight modes), incremental normalized vertical thrust command $\Delta(T/W)_{\text{cmd},V}$ (TMS in HFM), or pitch rate command q_{cmd} (TMS in TFM and HFM). The MCS outputs normalized thrust commands $(T/W)_{mp,\text{cmd}}$ and $(T/W)_{lp,\text{cmd}}$ for the main and lift propulsors, a nacelle angle command $\delta_{nac,\text{cmd}}$, and a longitudinal command $\xi_{lon,\text{cmd}} = \{\theta_{\text{cmd}},\ q_{\text{cmd}}\}$ comprising either a pitch attitude command θ_{cmd} or a pitch rate command q_{cmd}. For the roll axis, $\xi_{lat,\text{cmd}} = \{\phi_{\text{cmd}}, p_{\text{cmd}}\}$ can comprise either bank command or roll rate command respectively. For the yaw axis, $\xi_{dir,\text{cmd}} = \{r_{\text{cmd}},\quad \delta_{dir}\}$ comprises yaw rate command and a direct component from the pilot's pedal input.

The inner-loop controller is an explicit model-following (EMF) controller that employs feed-forward and feedback control action to track the attitude commands $\xi_{lat,\text{cmd}}, \xi_{lon,\text{cmd}}, \xi_{dir,\text{cmd}}$ by generating normalized control efforts $u_{lat}, u_{lon}, u_{dir} \in [-1, +1]$ about the respective axes. The EMF controller implementation follows [16]. The inverse propulsor models convert the main and lift propeller thrust commands into the necessary RPM command components $N_{0,mp}$ and $N_{0,lp}$ common to all main and lift propulsors. Differential thrust steering, used for taxiing on the ground in CTOL mode, generates a differential thrust command ΔN_{DT} between main propulsors 1, 2 and 3, 4.

2.4.1 Control Allocation

The control allocation logic generates commanded states for each control effector (Table 2), yielding the control vector

$$U_{\text{cmd}}^{16\times 1} = \{\delta_{f_1}, \delta_{f_2}, \delta_{f_3}, \delta_{f_4}, \delta_s, \delta_r, \delta_{t_1}, \delta_{t_2}, \delta_{t_3}, \delta_{t_4}, N_1, N_2, N_3, N_4, N_5, N_6\}^T$$

The flaperon deflections are computed as

$$\delta_{f_1} = \delta_{f_2} = -\delta_{f_3} = -\delta_{f_4} = \Delta\delta_{f,\phi} = \Delta\delta_f^{max,\phi}\ \zeta_{\phi,f}\ u_{lat} \tag{1}$$

The stabilator and rudder deflections are computed as

$$\delta_s = -\delta_s^{max}\ u_{lon}, \qquad \delta_r = +\delta_r^{max}\ u_{dir}$$

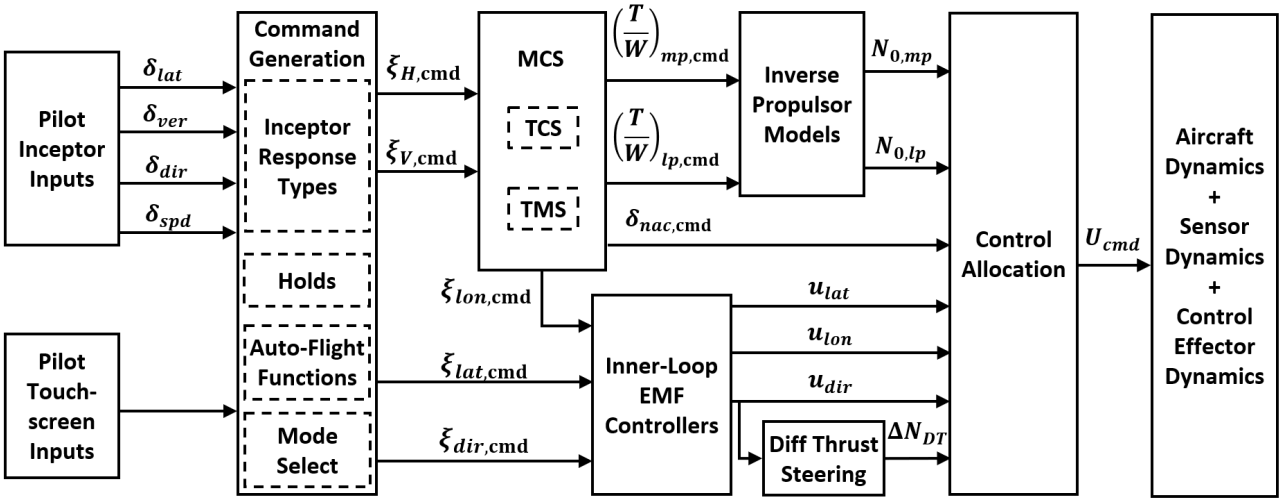


Figure 5 – Flight control system architecture

The nacelle tilt angles are computed as

$$\begin{bmatrix}\delta_{t_1}\\ \delta_{t_2}\\ \delta_{t_3}\\ \delta_{t_4}\end{bmatrix} = \begin{bmatrix}1.0 & -1.0\\ 1.0 & 0.0\\ 1.0 & 0.0\\ 1.0 & +1.0\end{bmatrix} \begin{bmatrix}\delta_{nac,\text{cmd}}\\ \Delta\delta_{nac,\psi}\end{bmatrix}, \qquad \Delta\delta_{nac,\psi} = \Delta\delta^{max}_{nac,\psi}\ \zeta_{\psi,nac}\ u_{dir} \tag{2}$$

Main and lift propeller RPM commands are computed as

$$\begin{bmatrix}N_1\\ N_2\\ N_3\\ N_4\end{bmatrix} = \begin{bmatrix}1.0 & +1.0 & 0.0 & +1\\ 1.0 & +1.0 & +1.0 & +1\\ 1.0 & -1.0 & +1.0 & -1\\ 1.0 & -1.0 & 0.0 & -1\end{bmatrix} \begin{bmatrix}N_{0,mp}\\ \Delta N_{\phi,mp}\\ \Delta N_{\theta,mp}\\ \Delta N_{\psi,mp}\end{bmatrix}, \qquad \begin{bmatrix}N_5\\ N_6\end{bmatrix} = \begin{bmatrix}1.0 & +1.0 & -1.0\\ 1.0 & -1.0 & -1.0\end{bmatrix} \begin{bmatrix}N_{0,lp}\\ \Delta N_{\phi,lp}\\ \Delta N_{\theta,lp}\end{bmatrix}$$

$$\begin{aligned}
\Delta N_{\phi,mp} &= \Delta N^{max}_{\phi,mp}\ \zeta_{\phi,mp}\ u_{lat}\\
\Delta N_{\theta,mp} &= \Delta N^{max}_{\theta,mp}\ \zeta_{\theta,mp}\ u_{lon}\\
\Delta N_{\psi,mp} &= \Delta N^{max}_{\psi,mp}\ \zeta_{\psi,mp}\ u_{dir} + \Delta N_{DT}\\
\Delta N_{\phi,lp} &= \Delta N^{max}_{\phi,lp}\ \zeta_{\phi,lp}\ u_{lat}\\
\Delta N_{\theta,lp} &= \Delta N^{max}_{\theta,lp}\ \zeta_{\theta,lp}\ u_{lon}
\end{aligned} \tag{3}$$

The computed control surface and nacelle deflections are subject to physical deflection limits. The wash-in/wash-out parameters in Eqs. 1, 2, 3 are scheduled with respect to nacelle angle per the schedule shown in Table 3.

3. System Identification Approach

The experimental design begins by using the MADCASP simulation model to obtain an initial estimate of the input parameters, such as frequency range of interest, amplitude, and record length. The input-generating blocks from the simulation are then transferred to a hardware model for system-identification flight tests.

3.1 Input Design

Various input types are designed for each axis to excite the aircraft dynamics and collect system-identification data. Two types of frequency-sweep inputs are employed, as shown in Fig. 6. The frequency-sweep input shown in Fig. 6(a) is based on the approach described by Tischler and Remple [17] and described mathematically as:

$$\begin{aligned}
K(t) &= C_2\left(e^{\frac{C_1 t}{T_{\text{rec}}}} - 1\right)\\
\omega(t) &= \omega_{\min} + K(t)\cdot(\omega_{\max} - \omega_{\min})\\
\theta(t) &= \int_0^t \omega(\tau)\, d\tau\\
\delta_{sweep}(t) &= A\cdot\sin(\theta(t))
\end{aligned} \tag{4}$$

Table 3 – Wash-in wash-out schedules (linear variations between data points)

δ_{nac}	90	80	70	60	50	40	$\leq$30
$\zeta_{\phi,mp}$	1	1	0.50	0	0	0	0
$\zeta_{\theta,mp}$	1	0.83	0.67	0.50	0.33	0.17	0
$\zeta_{\psi,mp}$	0	0	0.11	0.33	0.55	0.78	1
$\zeta_{\phi,lp}$	1	1	1	1	1	1	1
$\zeta_{\theta,lp}$	1	1	1	1	1	1	1
$\zeta_{\phi,f}$	1	1	1	1	1	1	1
$\zeta_{\psi,f}$	1	1	0.50	0	0	0	0
$\zeta_{\psi,nac}$	1	1	0.50	0	0	0	0

with the constants set to $C_1 = 4.0$ and $C_2 = 0.0187$.

The frequency of the sinusoidal input increases exponentially over time within a specified frequency range. Since the aircraft's dynamic characteristics are not fully known a priori, this input provides excitation across a broad frequency spectrum and helps identify the frequency range that contains the dominant aircraft dynamics. The resulting data are primarily used to estimate frequency-response data and to develop higher-order system (HOS) or lower-order equivalent system (LOES) models.

The discrete sine-sweep input shown in Fig. 6(b) consists of a sequence of constant-frequency sinusoidal inputs applied at multiple discrete frequencies spanning the frequency range of interest. Each frequency is maintained for several cycles so that the aircraft can reach a steady state at that frequency. T The resulting data are used to cross-check the frequency-response estimates obtained from the continuous sweep of Fig. 6(a).

To collect data for the time-domain studies, a sequence of step inputs is designed, as shown in Fig. 6(c). The magnitude and length of the input are adjusted so that data can be collected under different conditions (for example, at multiple bank angles), and the time between successive inputs is adjusted to allow the vehicle to reach a steady state before applying another step command.

3.2 System Identification Integration with the Control System

The programmed test inputs (PTIs) for system identification, δ_{sweep}, add to the trim values of normalized control inputs generated by the Explicit Model Following (EMF) inner-loop controller as shown in Fig. 7. To prevent the aircraft from drifting away from the hover trim state, the holds and automatic flight functions are used without interfering with PTIs. Additionally, the pilot can add input to the identified axis (in the case of single-axis excitation) or pass input to the other axes to adjust the vehicle's position or orientation. Table 4 summarizes the status of the stability and control augmentation system (SCAS) during the frequency sweep maneuvers. Because the aircraft is unstable in roll and pitch, feedback control on those axes remains enabled during sweeps on any axis. In contrast, yaw inputs are applied with the corresponding SCAS disabled. And the heave inputs are applied with TCS frozen at trim values before sweep, except for the nacelle angle.

3.3 Frequency Domain Model Identification

The frequency response characteristics of the data collected by using continuous frequency sweep (Fig. 6(a) are computed using MATLAB's `tfestimate` and `mscohere` functions to compute transfer functions and coherence metrics between excitation inputs and aircraft responses. Parametric transfer function models are then identified using MATLAB's `tfest` function to obtain low-order equivalent system (LOES) representations of the aircraft dynamics. The identified transfer functions are subsequently used to update the corresponding LOES elements within the EMF controller.

For the discrete sine-sweep inputs (Fig. 6(b)), the frequency response at each excitation frequency is estimated using a sinusoidal least-squares fit. The input and output signals corresponding to a given excitation frequency are first isolated and their mean values removed. Each signal is then approximated by

$$x(t) = A\sin(\omega t) + B\cos(\omega t), \tag{5}$$

where(ω) is the known excitation frequency and the coefficients(A) and (B) are obtained using linear least squares. The amplitude and phase of the fitted sinusoid are then computed as

$$M = \sqrt{A^2 + B^2}, \tag{6}$$

$$\phi = \tan^{-1}\left(\frac{B}{A}\right). \tag{7}$$

The frequency-response magnitude is estimated as the ratio of the output and input amplitudes,

$$|G(j\omega)| = \frac{M_y}{M_u}, \tag{8}$$

and the frequency-response phase is estimated as the difference between the output and input phases,

$$\angle G(j\omega) = \phi_y - \phi_u, \tag{9}$$

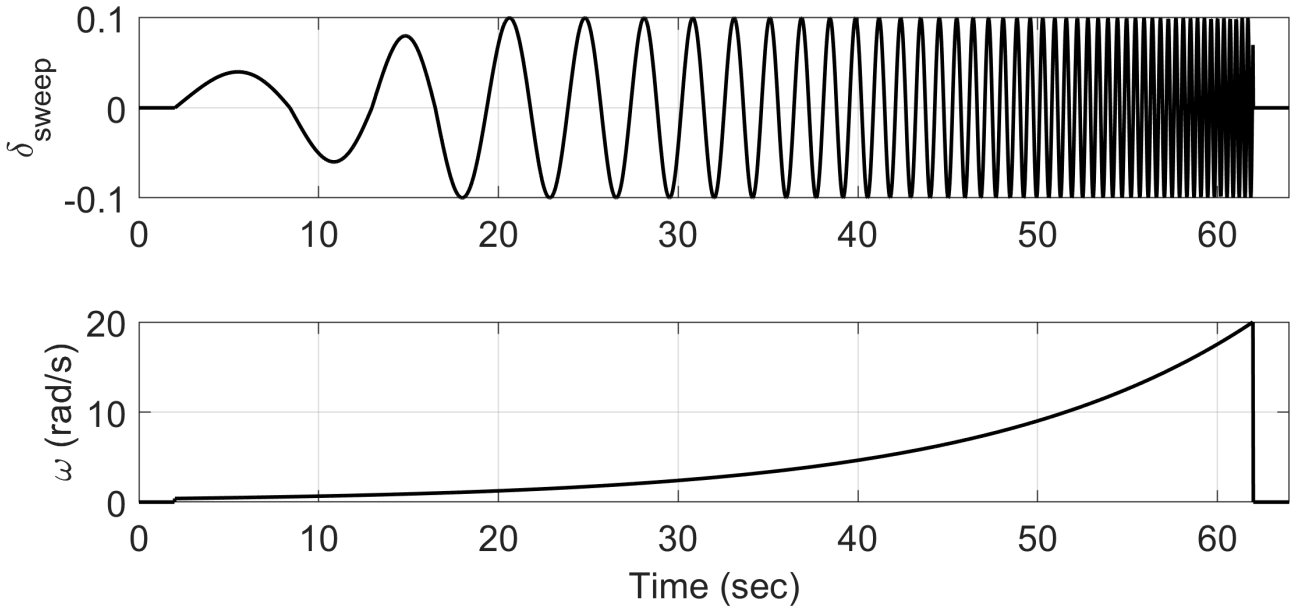
where the subscripts (u) and (y) denote the input and output signals, respectively. Repeating this process for each excitation frequency yields a set of discrete frequency-response points that can be used for frequency-domain system identification and validation of the identified dynamic models.

3.4 GCS interface for System Identification Inputs

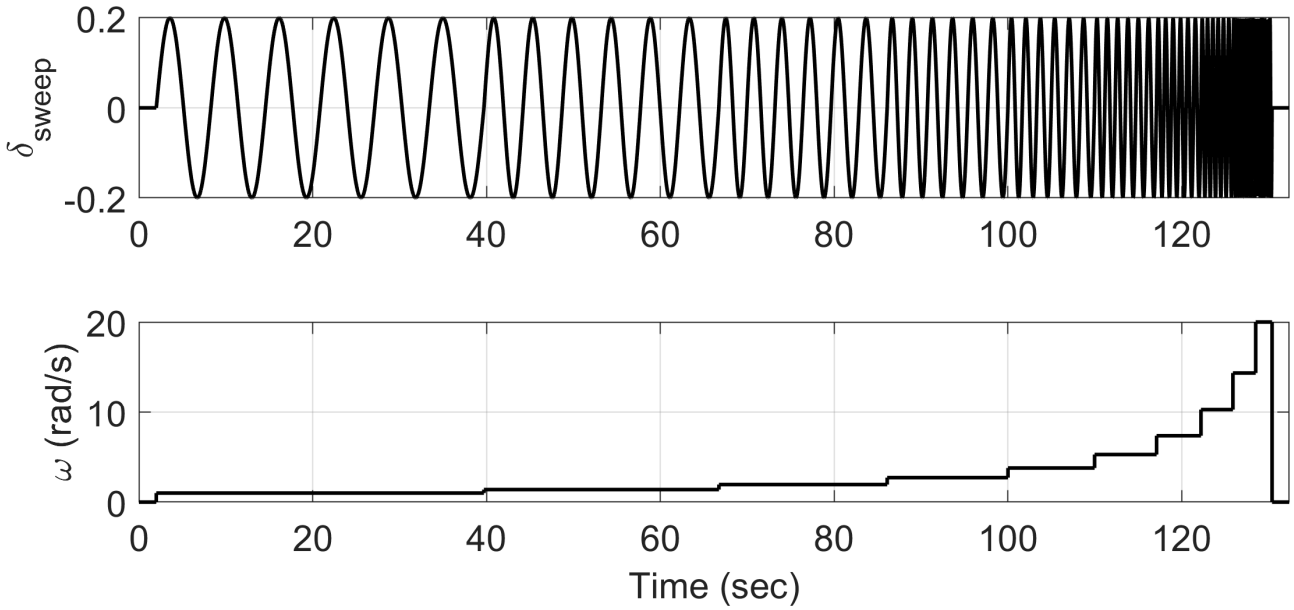
The programmed test input (PTI) for system identification purposes is activated using the touch interface on the GCS panel. Currently, each test input is designed to excite only one axis (roll, pitch, yaw, or heave) throughout the entire test duration. The touch interface shown in Fig 8 is used to activate a PTI. The desired axis is first selected using the **PROG GROUP** button. Pressing the '+' or '- ' buttons increments or decrements the number displayed on the screen. PROG GROUPs 1, 2, 3, and 4 correspond to roll, pitch, yaw, and heave axes, respectively. After selecting the axis, the desired input type is chosen by pressing one of the maneuver buttons (**M1-M5**), each corresponding to a type of test input. The selected button lights up upon the successful engagement of the system identification maneuver.

Table 4 – Status of SCAS during hover system identification

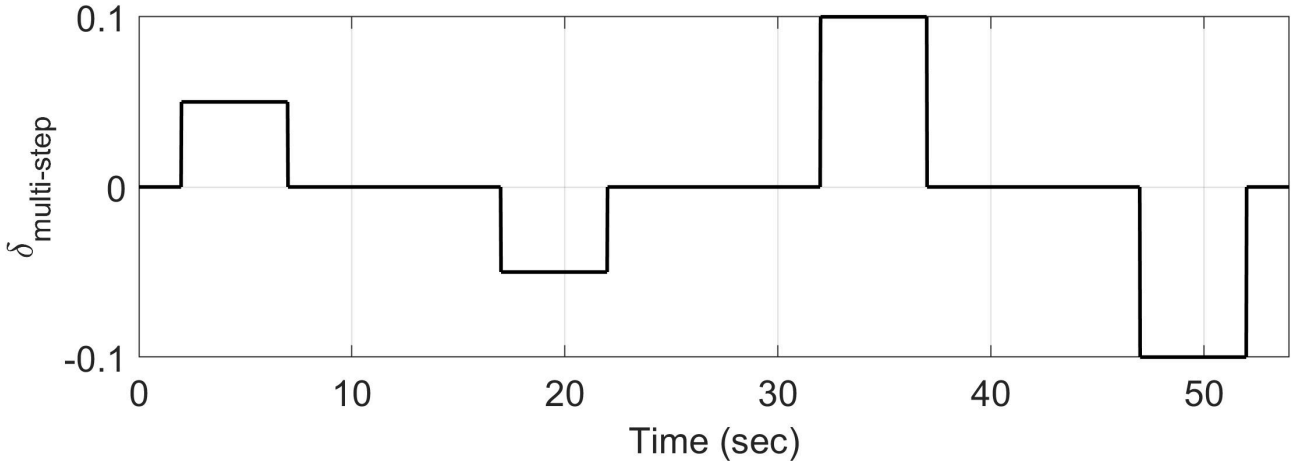
Axis	Roll (EMF)	Pitch (EMF)	Yaw (EMF)	Heave (TCS)
Roll	ON	ON	ON	ON
Pitch	ON	ON	ON	ON
Yaw	ON	ON	OFF	ON
Heave	ON	ON	ON	OFF



(a) Frequency sweep



(b) Discrete sine sweep



(c) Multi-step

Figure 6 – System identification excitation inputs.

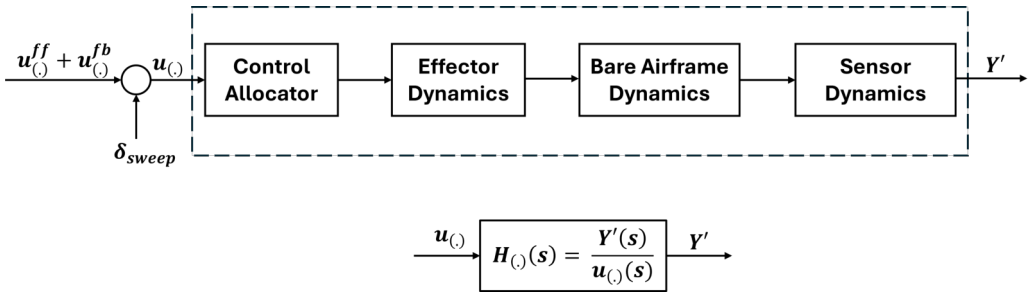


Figure 7 – System identification input integration with Explicit Model Following (EMF) controller

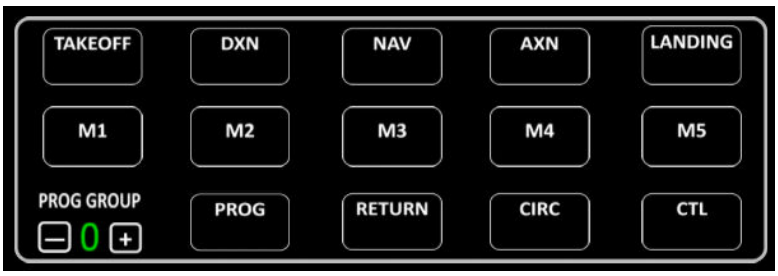


Figure 8 – Touch interface for activating programmed test inputs for system identification

4. Results

System identification maneuvers using the approach described in sec. 3. were performed in hover. The aircraft was first taken to a suitable altitude, and subsequently, programmed maneuvers were executed. The input parameters are listed in table 5 and table 6 for continuous and discrete sweep inputs, respectively. The identified higher-order system (HOS) and first-order lower-order equivalent system (LOES) are tabulated in table 7, along with the transfer functions obtained from the linear time-invariant (LTI) model from MADCASP.

Table 5 – Continuous frequency-sweep input parameters

Axis	**Magnitude**	$\omega_{\min}$ **(rad/s)**	$\omega_{\max}$ **(rad/s)**	T_{rec} **(s)**
Roll	0.2	0.4	20	60
Pitch	0.2	0.4	20	60
Yaw	0.3	1	20	20
Heave	0.2	1	20	20

Table 6 – Discrete frequency-sweep input parameters

Axis	**Amp.**	$\omega_{\min}$ **(rad/sec)**	$\omega_{\max}$ **(rad/sec)**	N_f	N_c
Roll	0.2	1	30	10	6
Pitch	0.2	1	30	10	6

Note: N_f is the number of excitation frequencies and N_c is the number of cycles at each frequency.

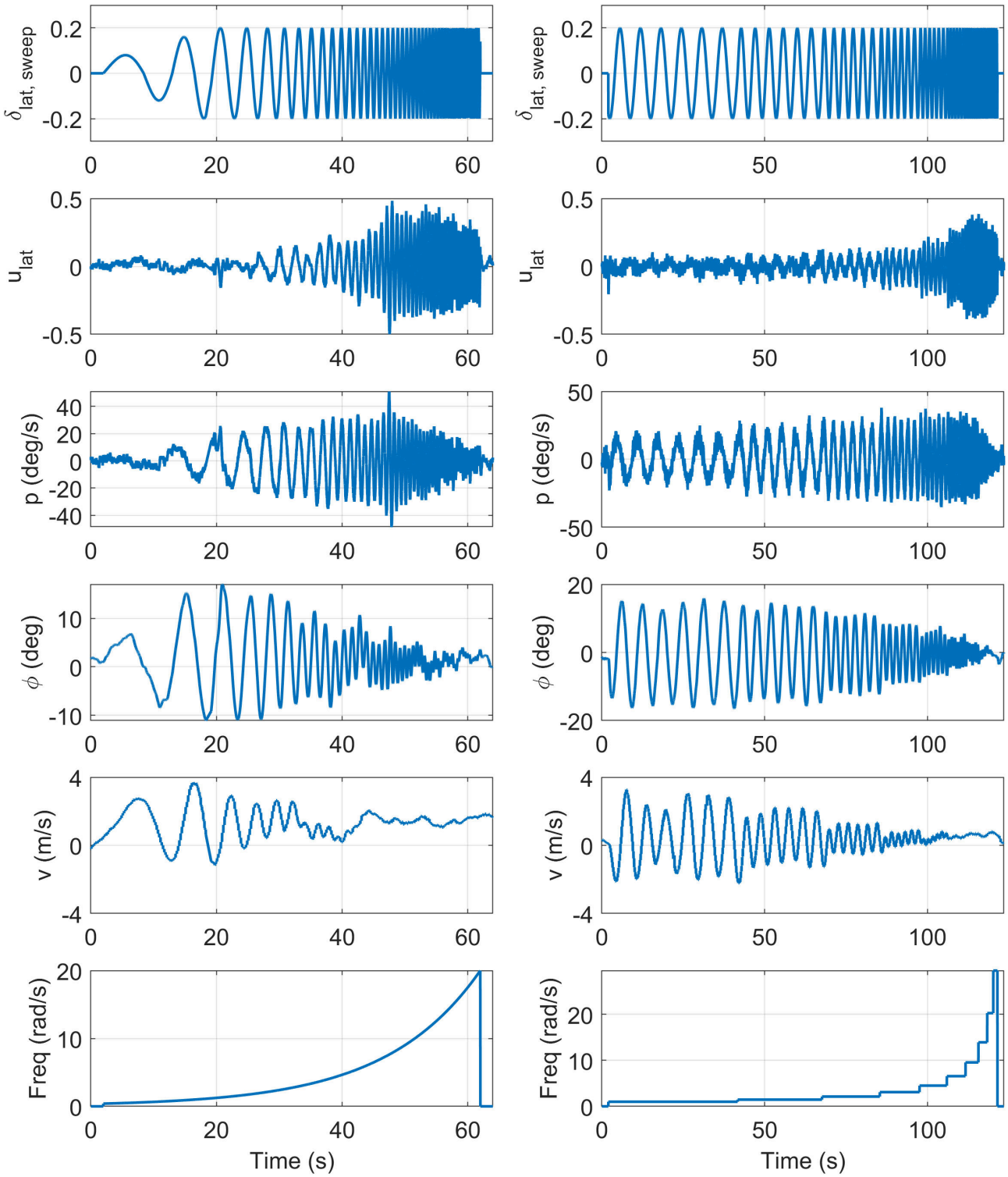
4.1 Roll Axis System Identification (Hover)

Two frequency sweep experiments are conducted: the first (Exp1) uses an input with continuously increasing frequency, and the second (Exp2) uses a sweep at discrete frequency points. Fig. 9(a) and Fig. 9(b) show the input, states, and the frequency time history during each experiment. In Exp1 (Fig. 9(a)), the input amplitude is gradually increased to its maximum value to limit vehicle excursions and prevent the aircraft from drifting excessively from the hover position. The control system strongly attenuates the response in the low-frequency region, resulting in relatively small roll-rate amplitudes at low excitation frequencies. As the excitation frequency increases, the roll rate increases in magnitude around 1.3 rad/sec, and the bank angle reaches its maximum amplitude, indicating the frequency range of the dominant roll dynamics. During the maneuver, the aircraft develops a lateral displacement in the direction of the initial input. Although subsequent inputs in the opposite direction induce motion back toward the original position, the net displacement remains biased toward the direction of the initial excitation.

In Exp2 (Fig. 9(b)), the input begins at 1 rad/s and excites the aircraft for six cycles at each frequency before advancing to the next frequency. As a result, the maneuver duration is significantly longer than that of the continuous frequency sweep. The roll-rate and bank-angle responses are observed immediately due to the higher initial excitation frequency.

The frequency-response data obtained from both sweep experiments are compared in Fig. 13. The two datasets show good agreement over most of the frequency range, with only minor differences at low frequencies, providing confidence in the accuracy of the identified response. The frequency response exhibits the characteristic hovering cubic behavior. A fourth-order higher-order system (HOS) identified from Exp. 1 captures the measured response well. In addition, a first-order lower-order equivalent system (LOES) is fitted over the approximately linear region of the log–log frequency-response plot to provide a simplified representation of the roll dynamics.

A kinematic consistency check was performed between the measured roll-rate response, $\frac{p(s)}{u_{lat}(s)}$, and the roll-attitude response, $\frac{\phi(s)}{u_{lat}(s)}$. A fourth-order transfer function was identified from the $\frac{\phi(s)}{u_{lat}(s)}$ frequency-response data and differentiated to obtain the corresponding roll-rate response in the frequency domain, $\frac{p(s)}{u_{lat}(s)} \approx \frac{s\phi(s)}{u_{lat}(s)}$. The resulting frequency response was compared with the measured



(a) Continuous frequency sweep (Exp1)

(b) Discrete frequency sweep (Exp2)

Figure 9 – Time history during frequency sweep in roll axis

Table 7 – Summary of flight identified (Flt) and simulation linear time invariant (LTI) models for hover

Model	**Roll** $\left(\frac{p(s)}{u_{lat}(s)}\right)$	**Pitch** $\left(\frac{q(s)}{u_{lon}(s)}\right)$	**Yaw** $\left(\frac{r(s)}{u_{dir}(s)}\right)$	**Heave** $\left(\frac{VV(s)}{\Delta N_{14}(s)}\right)$
Flt HOS	$\frac{12.733\ s(0.4502)(-0.3149)e^{-0.08s}}{(3.927)(0.679)[-0.452,\ 1.55]}$	$\frac{12.35\ s(-0.9237)(0.4636)e^{-0.08s}}{(3.147)(-0.1333)[-0.579,\ 1.76]}$	—	—
Flt LOES	$\frac{11.12\,e^{-0.08s}}{(0.1)}$	$\frac{8.973\,e^{-0.06s}}{(0.11)}$	$\frac{4.208\,e^{-0.14s}}{(0.6596)}$	$\frac{0.003754\,e^{-0.1s}}{(0.417)}$
LTI HOS	$\frac{12.342\ s(0.198)(0.0393)}{(1.084)(0.222)[-0.404,\ 0.878]}$	$\frac{11.692\ s([0.096,\ 0.028])}{(1.51)(0.2319)[-0.376,\ 1.19]}$	—	—
LTI LOES	$\frac{12.34}{(0.365)}$	$\frac{11.69}{(0.4086)}$	$\frac{4.571}{(0.1926)}$	$\frac{0.003013}{(0.2313)}$

Note: $[\zeta, \omega_n] = s^2 + 2\zeta\omega_n + w_m^2$, ζ = damping ratio, ω_n undamped natural frequency (rad/sec)
$(1/T) = s + 1/T$. Shorthand notation based on [18].

$\frac{p(s)}{u_{lat}(s)}$ data, as shown in Fig. 11. The good agreement observed indicates that the roll-attitude and roll-rate responses are kinematically consistent and that $\frac{s\phi(s)}{u_{lat}(s)}$ provides a reasonable approximation of $\frac{p(s)}{u_{lat}(s)}$. Since the transfer function identified from $\frac{\phi(s)}{u_{lat}(s)}$ yields a numerator in the standard form described by [16], the corresponding higher-order-system parameters are reported in Table 7.

4.2 Pitch Axis System Identification (Hover)

Similar to the roll axis sweeps, two experiments were conducted in the pitch axis, and the time histories are shown in Fig. 12(a). Similarly, higher-order and lower-order fits are obtained and reported in table 7.

4.3 Yaw Axis System Identification (Hover)

The time history data from the yaw axis sweep are shown in Fig. 14(a) and the frequency-response data are shown in Fig. 14(b). A first-order lower-order equivalent system (LOES) model was identified from the measured $\frac{r(s)}{u_{dir}(s)}$ frequency-response data by fitting the approximately linear region of the log–log frequency-response plot. The identified model provides a reasonable representation of the yaw-rate dynamics over the frequency range of interest. The resulting transfer-function parameters are summarized in Table 7.

4.4 Heave Axis System Identification (Hover)

The time domain and frequency domain data for the heave axis are shown in Fig. 15(a) and Fig. 15(b). The thrust-to-weight command was varied between ± 0.2 from hover thrust-to-weight. The resulting common main propeller rpm N_{14} is used as input for the transfer function identification. Consequently, a first-order lower-order equivalent system (LOES) model was identified from the $\frac{V_V(s)}{\Delta N_1 4(s)}$ frequency-response data by fitting the approximately linear region of the log–log frequency-response plot. The identified model provides a reasonable representation of the low-frequency vertical dynamics relevant to hover and low-speed flight. The resulting transfer-function parameters are summarized in Table 7.

4.5 Steady-State Vertical Velocity vs. Incremental RPM

To analyze steady-state vertical velocity $\dot{h}_{ss}$ versus incremental main propulsor RPM ΔN_{mp} relative to hover, three sets of vertical climb-and-descend maneuvers were conducted between altitudes of 20 ft

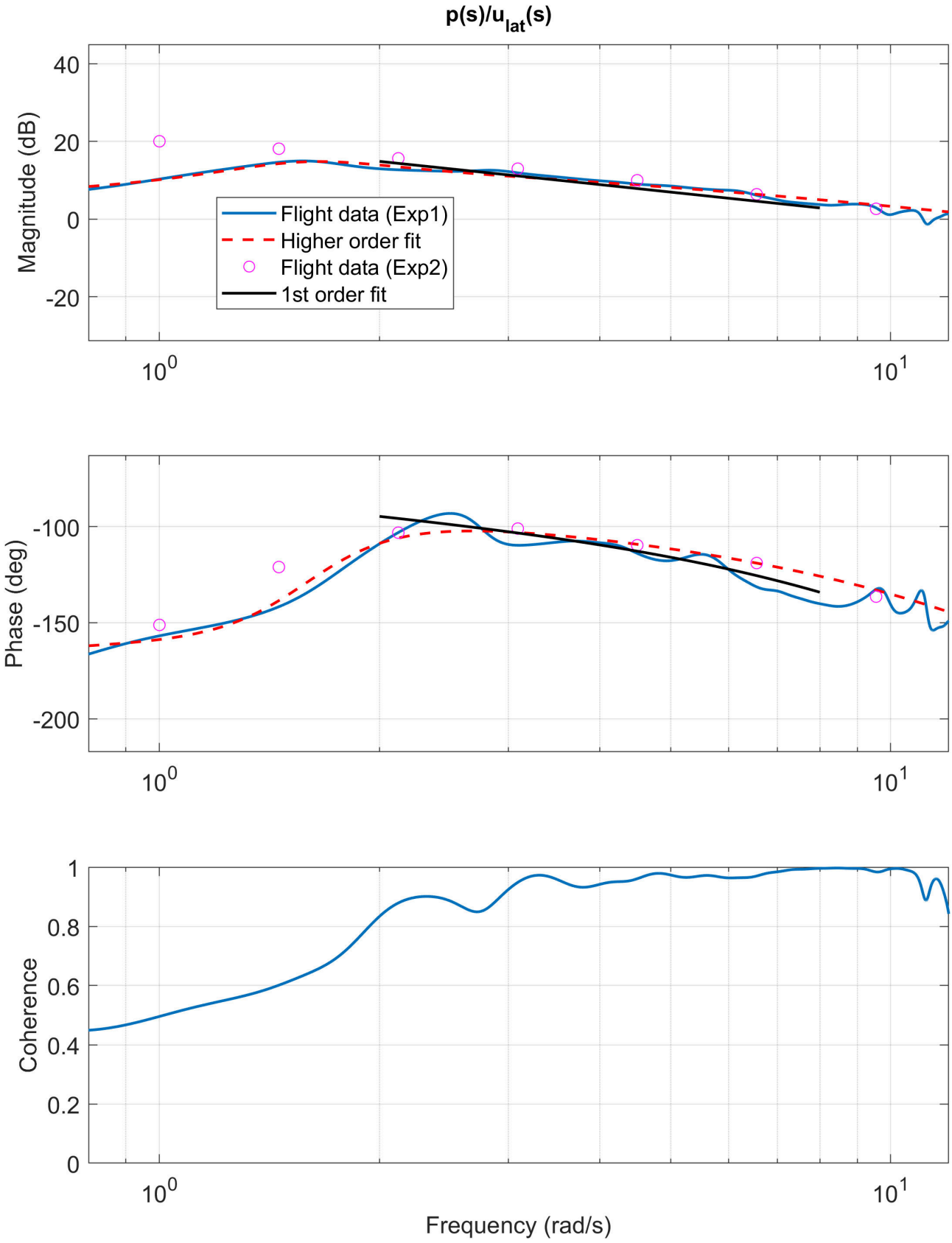


Figure 10 – Frequency response data and transfer function fit in roll axis

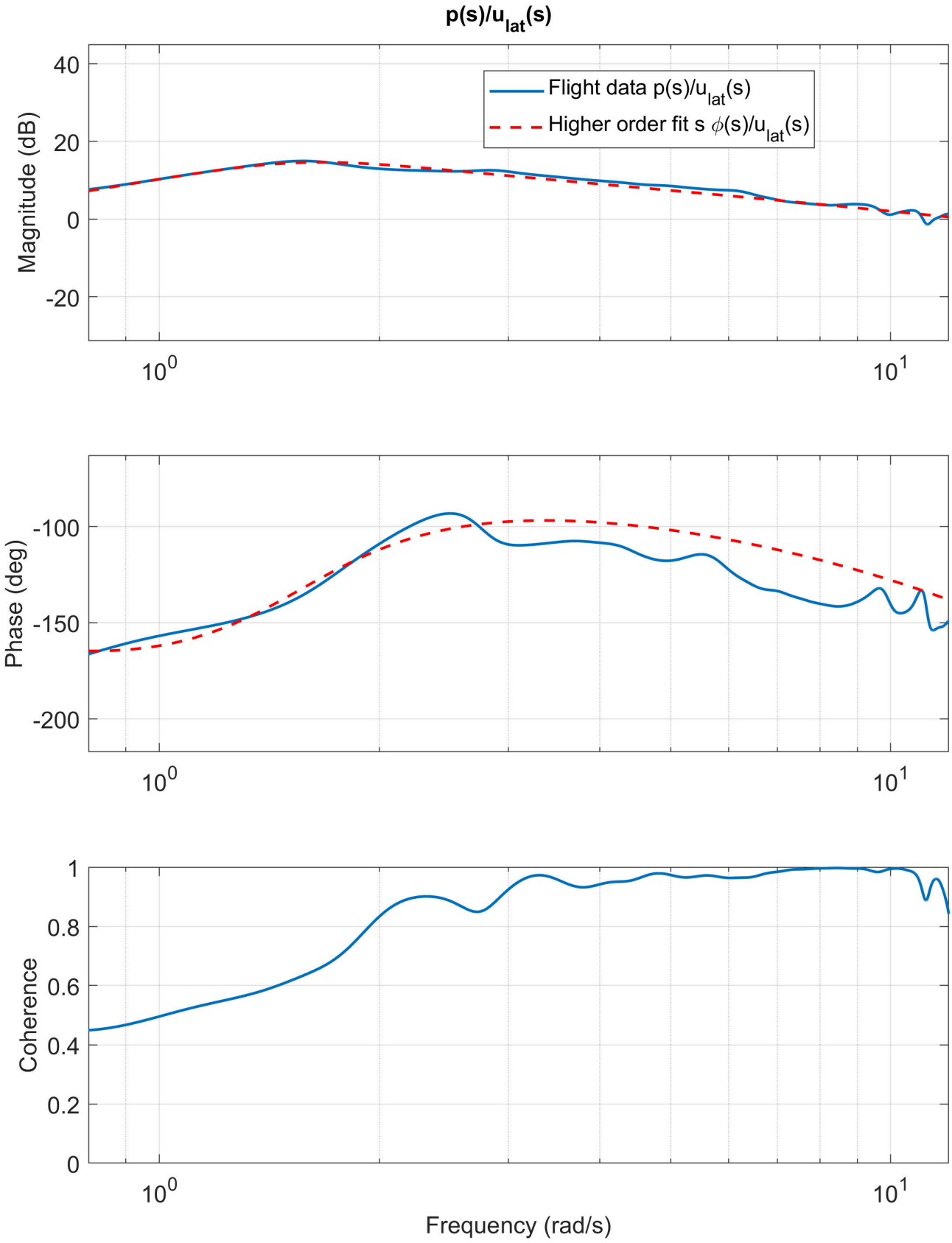
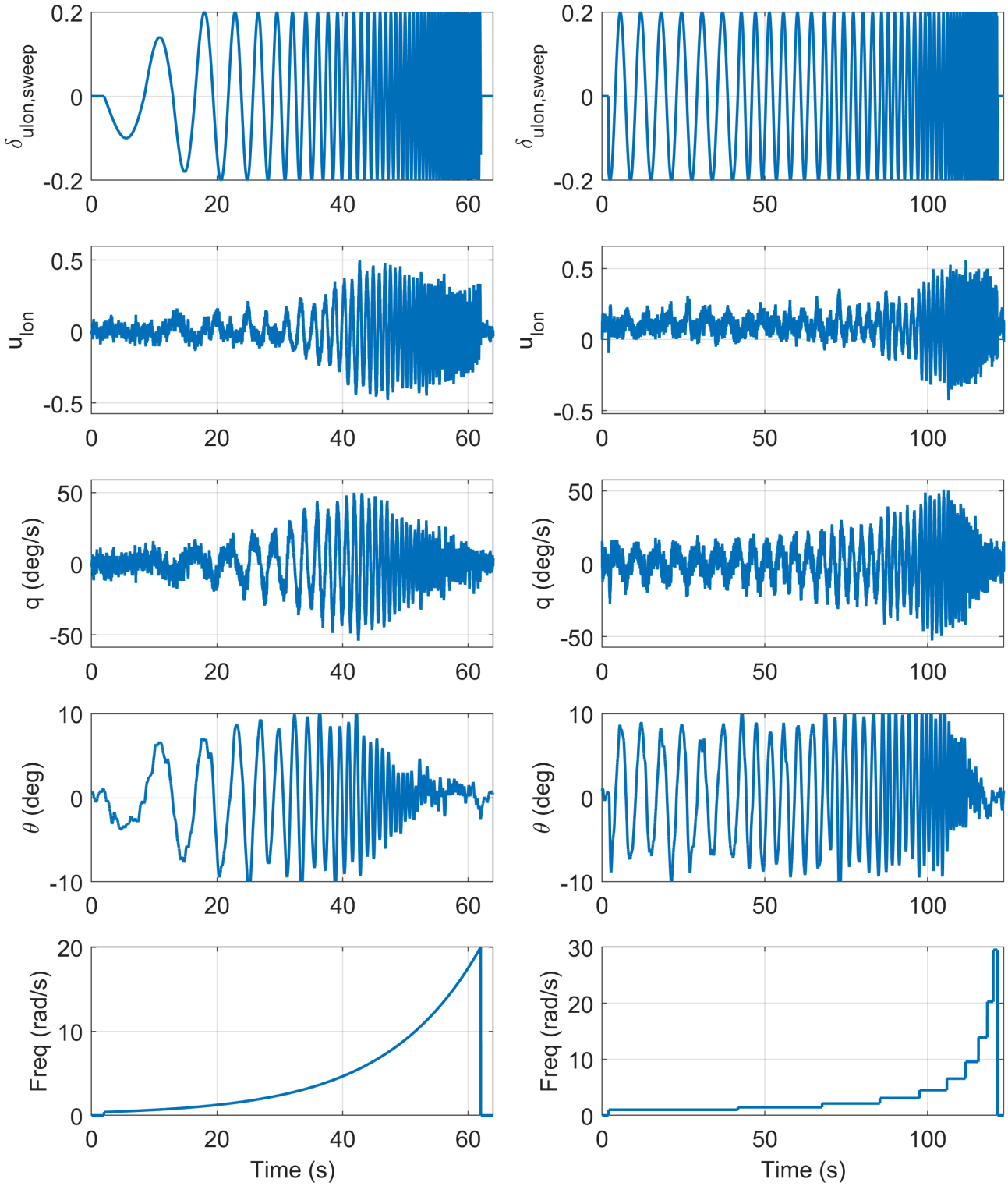


Figure 11 – Roll rate to lateral axis input flight data and transfer function fit



(a) Continuous frequency sweep (Exp1)

(b) Discrete frequency sweep (Exp2)

Figure 12 – Time history during frequency sweep in pitch axis

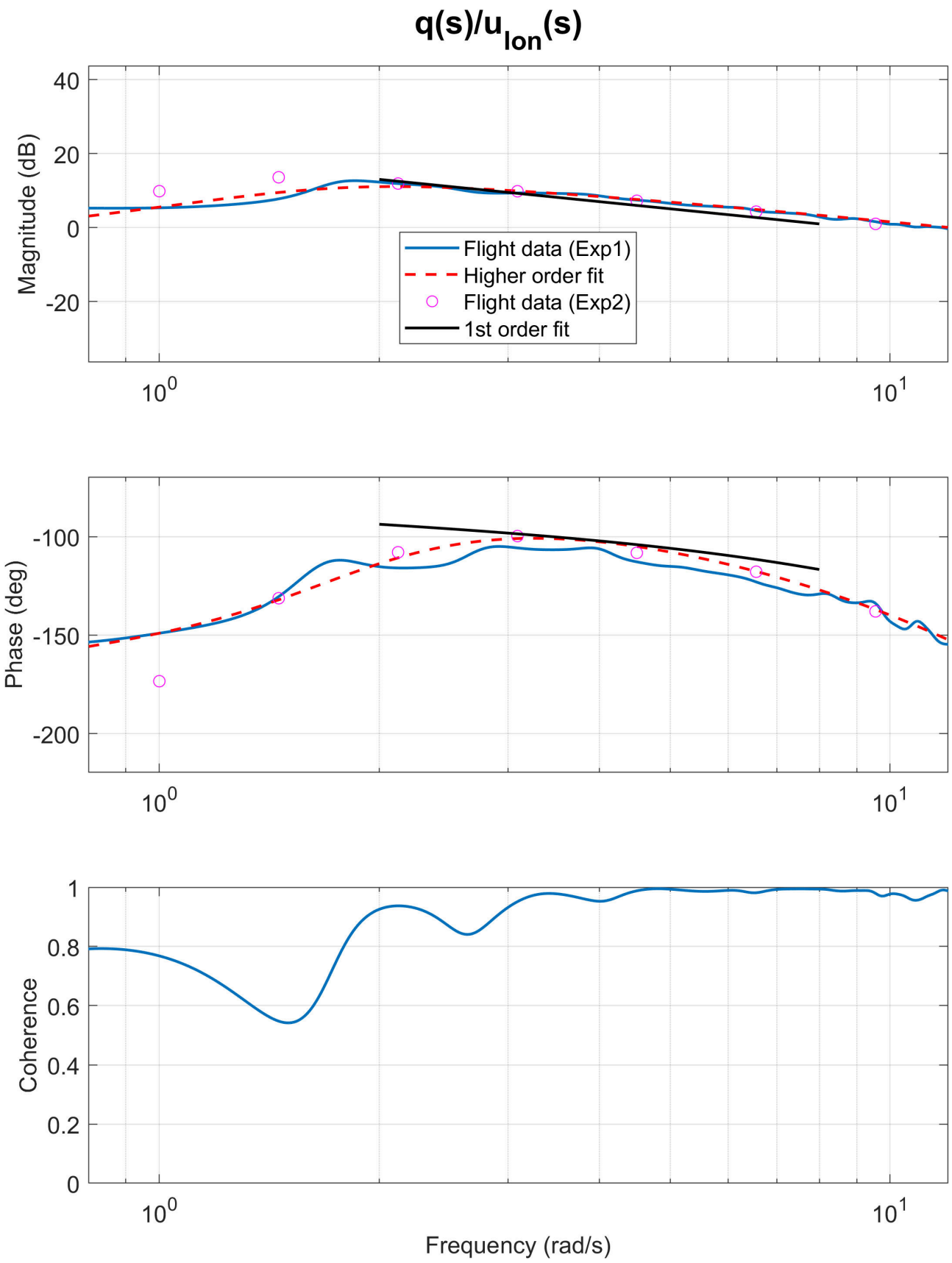
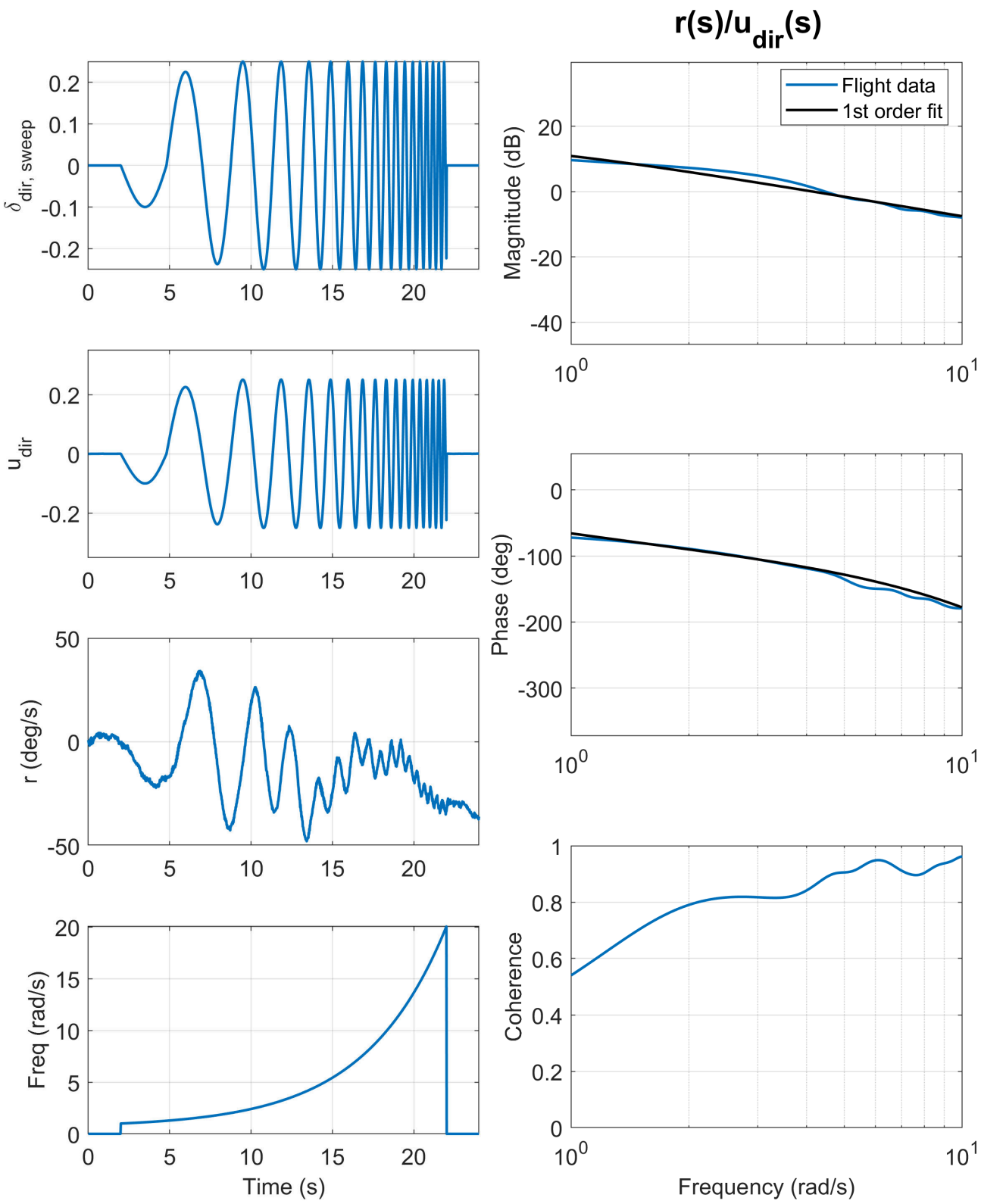


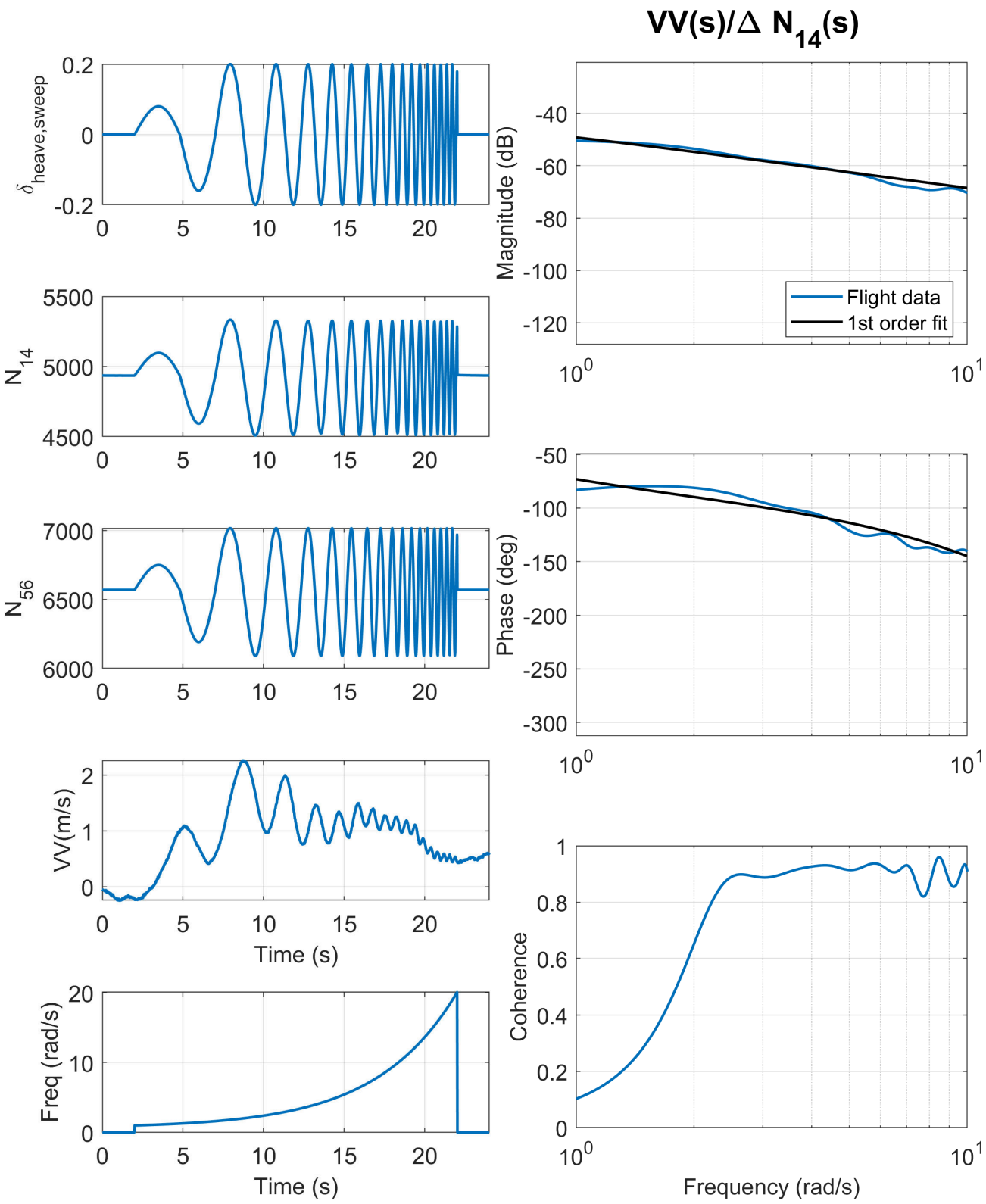
Figure 13 – Frequency response data and transfer function fit in pitch axis



(a) Time history during frequency sweep with continuous frequency input in yaw axis

(b) Frequency response data and transfer function fit in yaw axis

Figure 14 – System identification for the yaw axis



(a) Time history during frequency sweep with continuous frequency input in heave axis

(b) Frequency response data and transfer function fit in heave axis

Figure 15 – System identification for the heave axis

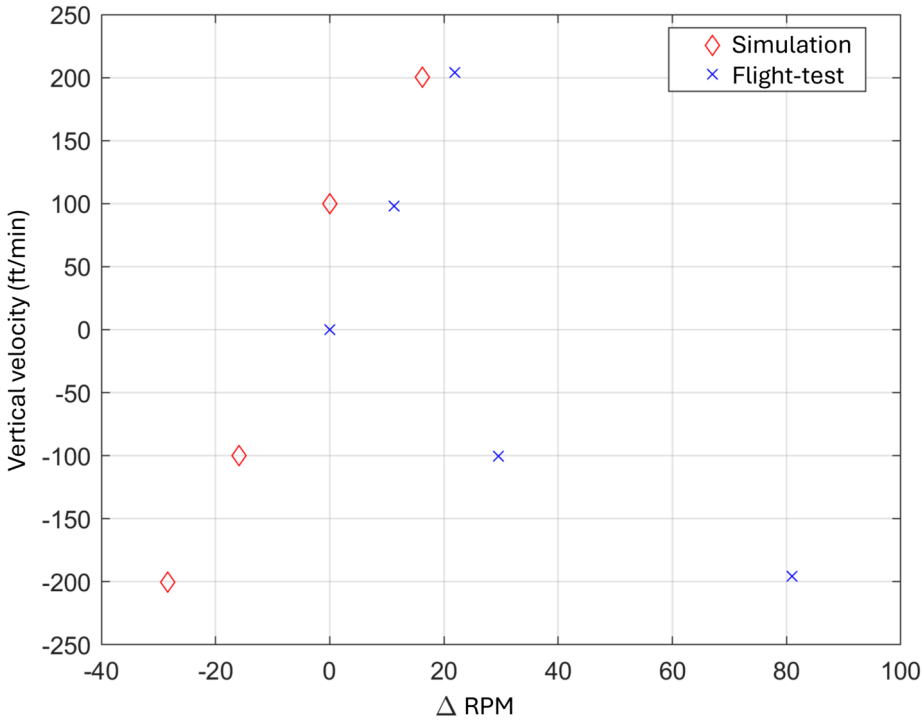


Figure 16 – Steady-state vertical velocity versus incremental main propulsor RPM

and 50 ft with commanded vertical velocity $\dot{h}_{\text{cmd}}$ of $\pm 100, \pm 200, \pm 300$ ft/min.

Steady-state conditions were identified using the nominal criteria in Table 8. The nominal $\dot{h}_{ss}$ error bound at hover was set to ± 15 ft/min. For climbs and descents, the nominal $\dot{h}_{ss}$ error bound was set to $\pm 5\%$ of $\dot{h}_{\text{cmd}}$ and a relaxed bound was set at $\pm 10\%$ of $\dot{h}_{\text{cmd}}$. Climbs and descents that did not satisfy the nominal or relaxed criteria were excluded from the analysis.

Fig. 16 shows $\dot{h}_{ss}$ as a function of ΔN_{mp} from flight-test as well as simulation. The hover RPM values were 4,360 RPM in simulation and 4,570 RPM in flight-test. During climbs, both show a trend of increasing ΔN_{mp} to sustain higher $\dot{h}_{ss}$. Further, the same step change in $\dot{h}_{ss}$ requires a greater increase in ΔN_{mp} at higher climb rates. In flight-test, a 100 ft/min climb required ΔN_{mp} of approximately $+8$ RPM, while the simulation model required $+12$ RPM. For a 200 ft/min climb in flight-test, $+20$ RPM was required, while in the simulation model, approximately $+28$ RPM was necessary.

Table 8 – Criteria used for selecting RPM data during steady-state climb and descent.

Maneuver	Criterion	$\dot{h}$ Error Bound	Duration (s)	Satisfied Cases
Hover	Nominal	± 15 ft/min	3	Hover
Climb & Descent	Nominal	$\pm 5\%$ $\dot{h}_{\text{cmd}}$	3	± 100, $+200$ ft/min
Descent	Relaxed	$\pm 10\%$ $\dot{h}_{\text{cmd}}$	3	-200 ft/min

During descents, however, the simulation model shows a reduction in steady-state RPM whereas flight-test data shows the opposite trend. Time history analysis of the initiation of the descents showed that there was a reduction in RPM to initiate the descents, followed by a higher-than-hover RPM to maintain the steady-state descent rate. This is likely due to the

4.6 Airspeed vs. Nacelle Angle

A flight in TMS control mode was performed, during which the pilot manually commanded nacelle angles in steps, increasing from 0° (forward flight) to 80° (near hover), with time between steps to allow the airspeed to reach a steady state. The steady-state airspeed versus nacelle angle is shown in Fig. 17. The simulation model was trimmed at the steady-state airspeed observed during the

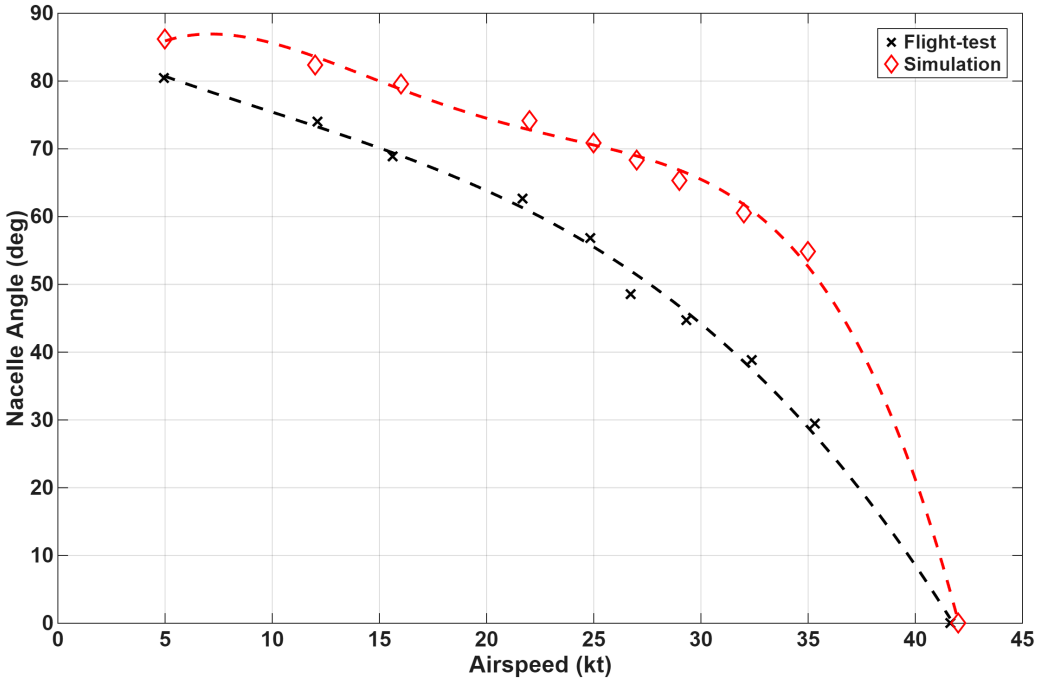


Figure 17 – Steady state airspeed vs nacelle angle

Table 9 – Calibration criteria

KEAS (kt)	Criterion	Constraint
≤ 35	$\theta_{nac,sim} \approx \theta_{nac,flt}$	-
> 35	$(T/W)_{H,sim} \approx (T/W)_{H,flt}$	$\theta_{nac} = 0°$

flight. Though the trend of nacelle angle versus airspeed is consistent, the baseline simulation model consistently predicts larger nacelle angles than those observed in flight-test, indicating an under-prediction of aerodynamic drag within the simulation model in hybrid flight mode.

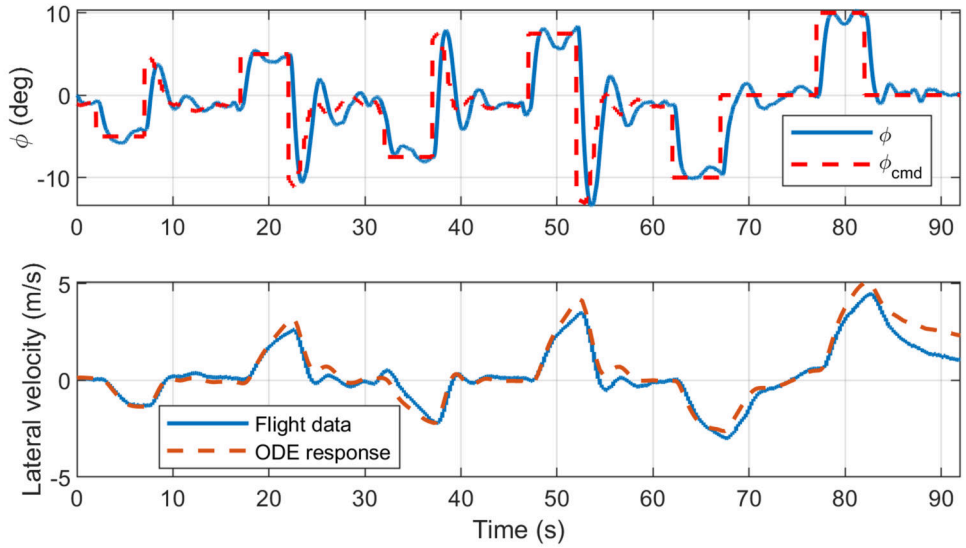


Figure 18 – Bank and lateral velocity time history

4.7 Lateral Velocity vs. Bank Angle

To determine the relationship between bank angle and steady-state lateral velocity while side-stepping, bank angle pulse commands of $5°, 7.5°, 10°$ were given alternately to the left and right (to allow can-

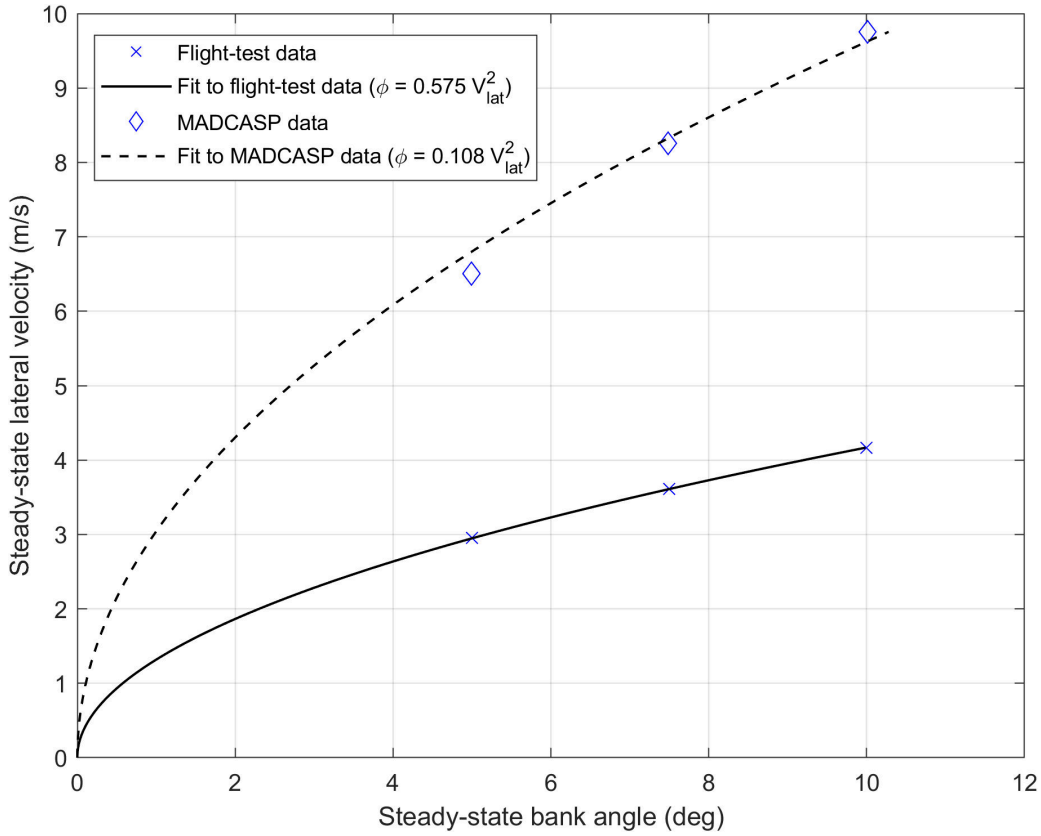


Figure 19 – Steady-state lateral velocity vs bank angle

cellation of the effect of wind). In between successive bank pulses, the aircraft banked opposite to the direction of lateral velocity to neutralize it. The bank pulses were held for 5 seconds each. However, post-flight analysis of the flight data (shown in Fig.18 showed that the pulse duration was insufficient to result in a true steady-state lateral velocity.

Therefore, an alternative analysis was attempted under the following assumptions: (i) a quadratic lateral drag relationship with respect to lateral velocity v_{lat}, (ii) thrust approximately equal to aircraft weight $W = mg$, (ii) a constant crosswind component v_w. Under these assumptions, the dynamics of lateral velocity are approximated as

$$\dot{v}_{lat}(t) = g\sin\phi(t) - \frac{K}{m}\{v_{lat}(t) + v_w\}^2 \tag{10}$$

This ordinary differential equation was solved with the bank angle time history $\phi(t)$ obtained from flight-test while iteratively changing the values of K and v_w to get a close match with the lateral velocity time history from flight-test. The best-match, shown in Fig.18, occurred with $K = 0.8023, v_w = -1.3$. Subject to the above assumptions, the steady-state lateral velocity as a function of bank angle can be found from the steady-state solution of Eq. 10 with zero wind as

$$\phi_{ss} = \sin^{-1}\left(\frac{Kv_{lat,ss}^2}{mg}\right) \tag{11}$$

Fig. 19 shows lateral velocity versus bank angle obtained based on Eq. 11 and that obtained from the MADCASP simulation model. While it is clear from the fits that a lateral drag model of the form Kv_{lat}^2 is appropriate, it is evident that there is substantial under-prediction of the lateral drag in the MADCASP simulation model. This warrants the incorporation of a calibration factor to internal drag calculations near $\approx 90^\circ$ sideslip conditions corresponding to side-stepping motion.

5. Conclusion

Flight-testing aimed at system identification of the characteristics of the VT-03-s Shadow subscale aircraft at/near hover were conducted and on-axis transfer functions about the roll, pitch, yaw, and

heave axes were identified. These were then compared to the transfer functions obtained from the MADCASP simulation model and its associated linearizations of the nonlinear flight dynamics model to identify where simulation model improvement is warranted. Flight-test data was also used to obtain steady-state relationships between nacelle angle and resultant airspeed, bank angle and resultant lateral velocity while sidestepping, and incremental propulsor RPM versus resulting vertical velocity. Comparisons of the above between flight-test data and simulation model predictions also revealed then need to calibrate the drag and possibly slipstream models within the simulation model to obtain better agreement with flight-test data.

6. Contact Author Email Address

Bikash Kunwar, email: bzk0067@auburn.edu

7. Copyright Statement

The authors confirm that they, and/or their company or organization, hold copyright on all of the original material included in this paper. The authors also confirm that they have obtained permission, from the copyright holder of any third party material included in this paper, to publish it as part of their paper. The authors confirm that they give permission, or have obtained permission from the copyright holder of this paper, for the publication and distribution of this paper as part of the ICAS proceedings or as individual off-prints from the proceedings.

References

[1] B. M. Simmons and K. A. Ackerman. Subscale tiltrotor evtol aircraft dynamic modeling and flight control software development. https://ntrs.nasa.gov/api/citations/20250003662/downloads/SimmonsEtAl_RS_FDC_Software_VFS81_v04282025.pdf, 2025. Accessed: 2025-11-09.

[2] B.J. German, A. Jha, S.K.S. Whiteside, and J.R. Welstead. Overview of the Research Aircraft for eVTOL Enabling techNologies (RAVEN) Activity. In *AIAA AVIATION 2023 Forum*, San Diego, CA, June 2023. AIAA-2023-3924.

[3] B.M. Simmons and S.C. Geuther. Validation of a Mid-Fidelity Approach for Aircraft Stability and Control Characterization. In *AIAA AVIATION 2023 Forum*, San Diego, CA, June 2023. AIAA-2023-4076.

[4] I. Chakraborty, B. Kunwar, S.H. Putra, R. Bhandari, and H.C. McCormick. Flight Testing of the VT-03-s Shadow Multi-Tilt-Rotor Configuration with a Maneuver Control System Enabling Simplified Vehicle Operations and Tactical Maneuvering. In *Vertical Flight Society (VFS) Forum 82*. Paper 229, May 2026.

[5] Mark B. Tischler and Robert K. Remple. *Aircraft and rotorcraft system identification*. American Institute of Aeronautics and Astronautics Reston, VA, 2012.

[6] Eugene A. Morelli and Vladislav Klein. *Aircraft system identification: theory and practice*, volume 2. Sunflyte Enterprises Williamsburg, VA, 2016.

[7] Benjamin M. Simmons, James L. Gresham, and Craig A. Woolsey. Flight-Test System Identification Techniques and Applications for Small, Low-Cost, Fixed-Wing Aircraft. *Journal of Aircraft*, 60(5):1503–1521, 2023. _eprint: https://doi.org/10.2514/1.C037260.

[8] Ravindra Jategaonkar, Dietrich Fischenberg, and Wolfgang von Gruenhagen. Aerodynamic Modeling and System Identification from Flight Data-Recent Applications at DLR. *Journal of Aircraft*, 41(4):681–691, 2004. _eprint: https://doi.org/10.2514/1.3165.

[9] NASA. Research Aircraft for eVTOL Enabling techNologies (RAVEN), March 2025.

[10] Bikash Kunwar, Aashutosh A Mishra, and Imon Chakraborty. Sizing and analysis of canard-wing aircraft with jet propulsion. In *AIAA AVIATION FORUM AND ASCEND 2024*, page 3752, 2024.

[11] Imon Chakraborty and Aashutosh Aman Mishra. Sizing of Tilt-Wing Aircraft with All-Electric and Hybrid-Electric Propulsion. *Journal of Aircraft*, 60(1):245–264, January 2023.

[12] John Deyoung. Theoretical symmetric span loading due to flap deflection for wings of arbitrary plan form at subsonic speeds, January 1952. NTRS Author Affiliations: NTRS Report/Patent Number: NACA-TR-1071 NTRS Document ID: 19930092116 NTRS Research Center: Legacy CDMS (CDMS).

[13] RD Finck. Usaf (united states air force) stability and control datcom (data compendium). Technical report, MCDONNELL AIRCRAFT CO ST LOUIS MO, 1978.

[14] Jinggen Zhao. *Dynamic Wake Distortion Model for Helicopter Maneuvering Flight*. PhD thesis, Georgia Institute of Technology, Atlanta, GA, USA, March 2005.

[15] Advanced Precision Composites Propellers. Apc propeller performance data. Online: `https://www.apcprop.com/technical-information/performance-data/`, 2024.

[16] M. Tischler, T. Berger, C. Ivler, M. Mansur, K. Cheung, and J. Soong. *Practical Methods for Aircraft and Rotorcraft Flight Control Design - An Optimization-Based Approach*. American Institute of Aeronautics and Astronautics, 1st edition, 2017.

[17] M. Tischler and R. Remple. *Aircraft and Rotorcraft System Identification - Engineering Methods with Flight Test Examples*. American Institute of Aeronautics and Astronautics, 2nd edition, 2012.

[18] Mark B. Tischler and Juergen Kaletka. MODELING XV-15 TILT-ROTOR AIRCRAFT DYNAMICS BY FREQUENCY AND TIME-DOMAIN IDENTIFICATION TECHNIQUES by Mark B.Tischler Aeroflightdynamics Directorate.